ADVANCED FUNCTIONAL MATERIALS
www.afm-journal.de

A Bio-Inspired Rod-Shaped Nanoplatform for Strongly Infecting Tumor Cells and Enhancing the Delivery Efficiency of Anticancer Drugs

*Dan Li, Zhaomin Tang, Yuqian Gao, Huili Sun, and Shaobing Zhou**

The rapid clearance of circulating nanocarriers in blood during systemic drug delivery remains a challenging hurdle in cancer chemotherapy. Here, inspired by the unique features of bacterial pathogens, an original biodegradable polymer micellar system with a rod-like shape similar to the morphology of bacterial pathogens is developed. These novel nanocarriers have excellent features such as a great capacity of overcoming the rapid clearance of reticuloendothelial system (RES) with long blood circulation, high cellular internalization, and enhanced therapeutic efficacy against cancers. In vivo pharmacokinetic studies in mice reveal that the rod-like micelles of ≈40 nm in diameter and 600 nm in length possess a minimal uptake by the RES and excellent blood circulation half-lives ($t_{1/2\beta}$ = 24.23 ± 2.87 h) for carrying doxorubicin in contrast to spheres ($t_{1/2\beta}$ = 8.39 ± 0.53 h). The antitumor activity of the rod-shaped micelles in Balb/c mice bearing H22 tumor xenograft models reveals that they are promptly internalized by tumor cells, resulting in their superior potency and efficacy against artificial solid tumors. These findings suggest that the bio-inspired nanocarriers as an emerging drug delivery platform may have considerable benefits for enhancing the delivery efficiency of anticancer drugs and in turn enhancing cancer therapy in future clinical applications.

1. Introduction

Nanoparticles (NPs) have shown enormous prospects as carriers in drug and gene delivery because they have the ability to carry drugs directly to the diseased areas.[1,2] These nanocarriers are generally administered via intravenous (i.v.) injection and subsequently encounter numerous barriers, including the walls of blood vessels, the physical entrapment of particles in organs, and the removal of particles by phagocytic cells.[3] As a result, the majority of injected nanocarriers end up in the liver and spleen, and only a small percentage (1%–10%) of nanocarriers accumulate in tumor sites.[4] The low delivery efficiency of these therapeutic agents has undoubtedly resulted in the poor efficacy of anticancer treatments. Currently, the rapid clearance of circulating nanocarriers during systemic drug delivery remains a challenging hurdle for cancer chemotherapy.

To address this challenge, the physicochemical parameters of NPs such as size[2,5–8] and surface chemistry[9–14] have been widely investigated. More recently, another important parameter, particle shape, has received significant attention because it controls the interaction of NPs with cells and the systemic distribution of NPs, thus having a profound effect on their performance.[3,4,15–23] In nature, viruses[4] and bacterial pathogens[24] with various asymmetric geometries have great capabilities of infecting specific cell types. This is especially the case for bacterial pathogens, such as the Gram-negative bacteria *Salmonella* and the Gram-positive bacterium *Listeria monocytogenes*, which have rod-like shapes that can promote their entry into nonphagocytic mammalian cells.[24,25] Inspired by the unique ability of these bacterial pathogens, we developed biodegradable polymer micelles with precisely controlled rod-like shapes for the enhanced infection and killing of targeted tumor cells.

Some drug delivery applications have proposed that NPs with elongated shapes have more advantages as nanocarriers in comparison to spherical NPs.[26–28] Despite these pioneering studies, there is still a shortage of a comprehensive understanding of the interactions between the nanostructures and biological systems. Obtaining nanocarriers with well-defined nanostructures such as rod-like shapes is crucial to study the interactions between micelle shapes and biological systems. Several approaches for preparing nonspherical polymeric particles have been developed, including mechanical stretching,[29] emulsions,[30] microfluidics,[31] template-based synthesis,[3] and self-assembly.[32,33] Of these approaches, the self-assembly of amphiphilic copolymers into diversely shaped polymer micelles has received the most attention. Altering the morphology of micelles in a controlled manner is of great interest due to the potential advantages and applications of these micelles in the field of drug delivery. Micelle morphology can be affected by several factors, including chain architecture,[34–37] concentration,[38] solvent conditions (e.g., solvent selectivity,[32,39] CO_2,[40] temperature,[41] pH,[42] salt concentration,[43] small molecular surfactants,[44] and the hydrophilic/hydrophobic ratio.[45] The addition of ions into an aqueous solution is a simple and effective strategy for

D. Li, Dr. Z. M. Tang, Y. Q. Gao, Dr. H. L. Sun, Prof. S. B. Zhou
Key Laboratory of Advanced Technologies of Materials
Ministry of Education
School of Materials Science and Engineering
Southwest Jiaotong University
Chengdu 610031, P. R. China
E-mail: shaobingzhou@swjtu.edu.cn

DOI: 10.1002/adfm.201503664

inducing the transformation of the polymer micelles from a spherical shape to a rod shape. Furthermore, the inorganic salts that are generally used in this technique are components of biological environments and are nontoxic to the body.

In this study, we developed a novel bio-inspired rod-shaped polymer micellar system to improve drug delivery efficiency and, consequently, enhance cancer therapy by simply changing the concentration of NaCl in the micelle-containing solution. The polymer micelles with spherical (S), short rod-like (SR), and long rod-like (LR) shapes were formed via self-assembly of amphiphilic mPEG-PCL copolymers by adjusting the salt concentration of the solution (**Scheme 1**A). After i.v. injection,

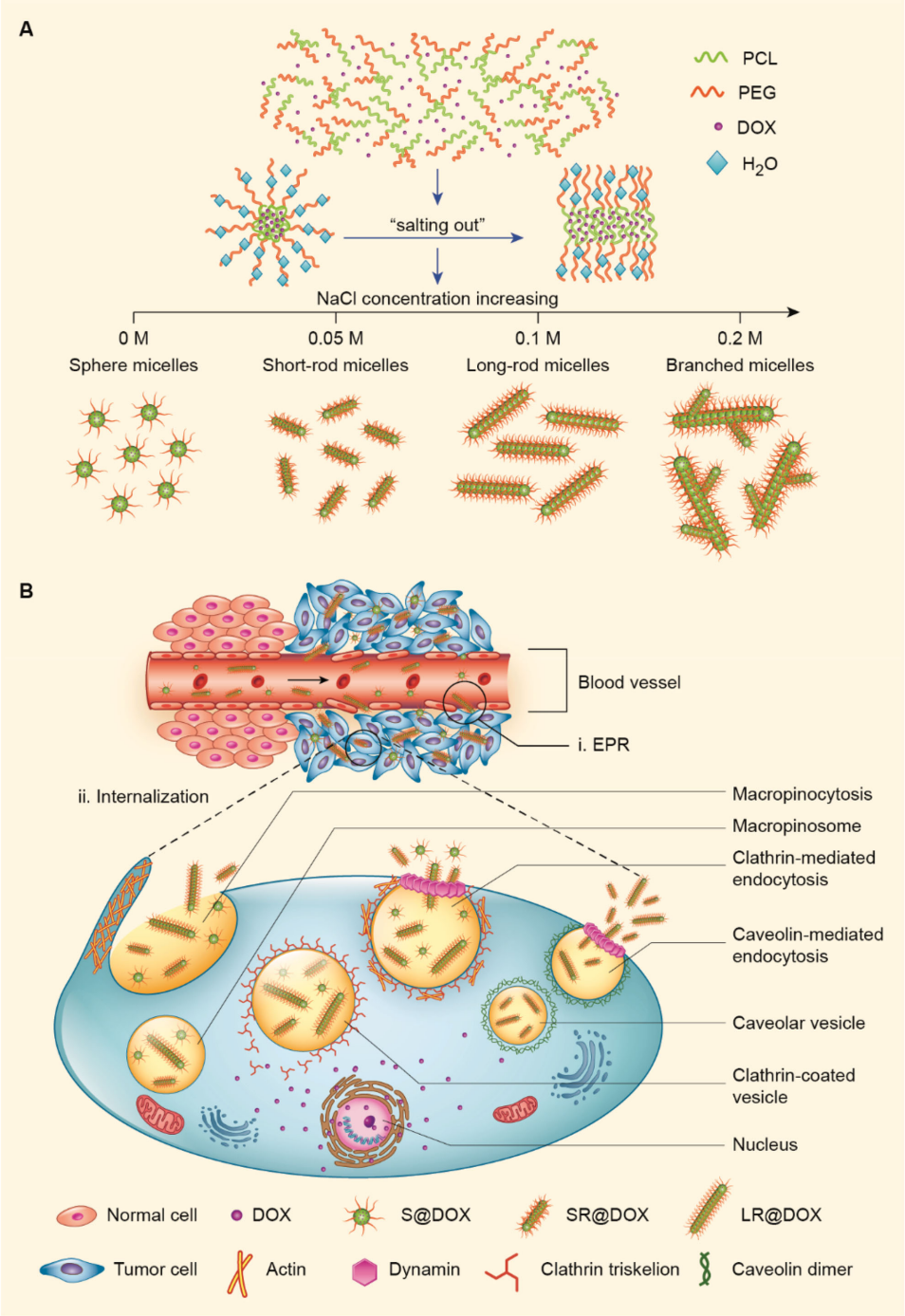

Scheme 1. Illustrated design concepts of bio-inspired drug-loaded polymer micelles with various morphologies and their schematically cellular internalizations. A) Self-assembly of the mPEG-CL_{41} block copolymer into diverse-shaped micelles under increasing concentration of NaCl. B) The delivery procedure of the DOX-loaded micelles (S@DOX, SR@DOX, and LR@DOX) from the blood circulation to the tumor tissues and finally to the tumor cells: i) accumulation at the tumor site via the EPR effect; ii) shape-dependent internalization.

these doxorubicin (DOX)-loaded nanocarriers with various shapes can accumulate spontaneously in tumor tissue through the enhanced permeability and retention (EPR) effect; later, they are internalized through diverse cellular uptake pathways; finally, the therapeutic agent is delivered and released into the organelles (Scheme 1B).

2. Results and Discussion

2.1. Morphology Optimization

To achieve micelles with well-defined rod-like shapes that were similar to the structures of bacterial pathogens, we first optimized the concentration of NaCl in the solution to assess its influence on the shape of the micelles. In transmission electron microscopy (TEM) and atomic force microscopy (AFM) images, respectively, in Figures S1 and S2 (Supporting Information), without NaCl, only spheres were acquired; As the concentration of NaCl in solution was increased to 0.05 M, the spherical micelles disappeared, eventually resulting in only rod-like micelles; As the concentration of NaCl changed from 0.05 to 0.1 M, the rod-like micelles elongated, and the length increased from ≈300 nm to more than 600 nm; Finally, when the concentration was increased from 0.1 to 0.2 M, the rod-like shape gradually turns into a branched shape. The most likely cause of the sphere-to-rod or rod-to-branched transformations was the "salting-out" of the PEG block by different concentrations of NaCl,[43] as schematically depicted in Scheme 1A.

Among these morphologies, the SR and LR nanostructures were selected as anticancer drug nanocarriers for all of the following investigations because their morphologies were the closest to the structures of bacterial pathogens. The spherical micelles were used as the controls in each experiment. The TEM images in **Figure 1** show that the diameters of the homogeneous spherical micelles were almost 80 nm (Figure 1A1,A1′). The SR micelles were ≈20 nm in diameter and 300 nm in length (Figure 1B1,B1′), whereas the LR micelles were ≈40 nm in diameter and 600 nm in length (Figure 1C1,C1′). These structures were further confirmed by confocal fluorescence microscopy (FM) after the micelles were loaded with Nile red, a hydrophobic fluorescent dye (Figure 1A2–C2,A2′–C2′). The diameter distributions (Figure S3A, Supporting Information) showed that the average diameters of the samples were 96 ± 3.1 nm for S, 132 ± 3.8 nm for SR, and 202 ± 6.1 nm for LR.

2.2. In Vitro Stability and Drug Release

To investigate the influences of both 0.9% physiological saline solution and the storage period on the stability of various shaped micelles, 1 mg mL^{-1} of the S, SR, and LR micelles was added to separate solutions of 0.9% NaCl. The stability of the micelles was studied by dynamic light scattering (DLS) at different time points, and visual comparisons were made between the freshly prepared micelles and the micelles stored for 120 h. As shown in **Figure 2**C, the appearance of all solutions was still transparent without aggregation at 120 h. The mean sizes (Figure 2B) and size distributions (Figure 2A) of the S, SR, and LR samples changed negligibly within 120 h, suggesting that the micelles had good stability in the 0.9% physiological saline

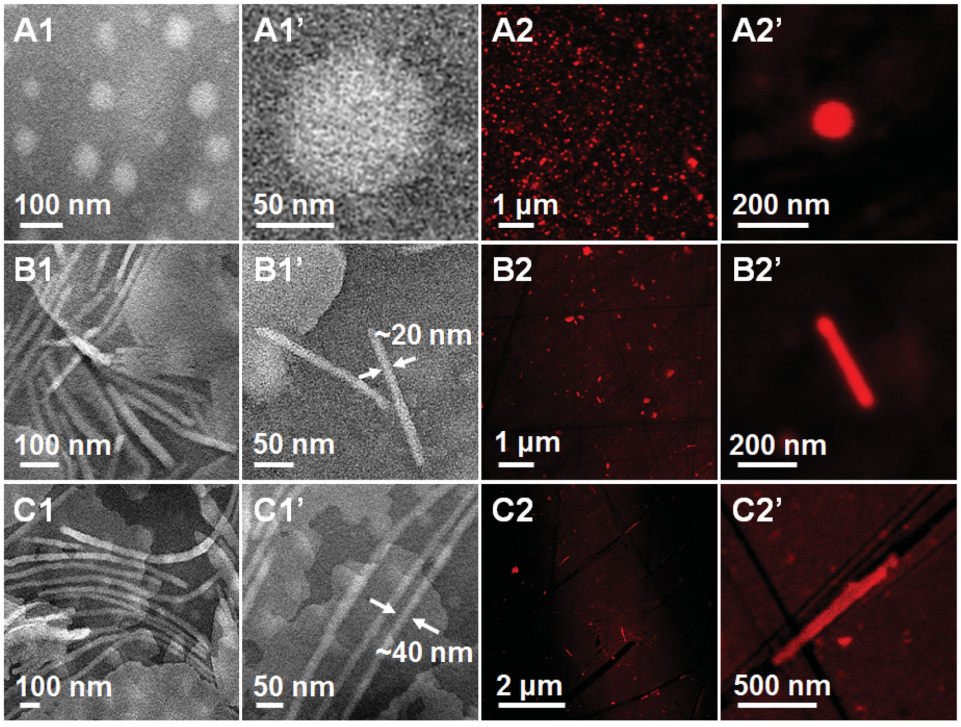

Figure 1. Micellar morphology observed with TEM and CLSM. A1,A2) Spherical (S); B1,B2) short rod-like (SR); C1,C2) long rod-like (LR) micelles. The nanostructures were loaded with 2.5% Nile red for confocal imaging.

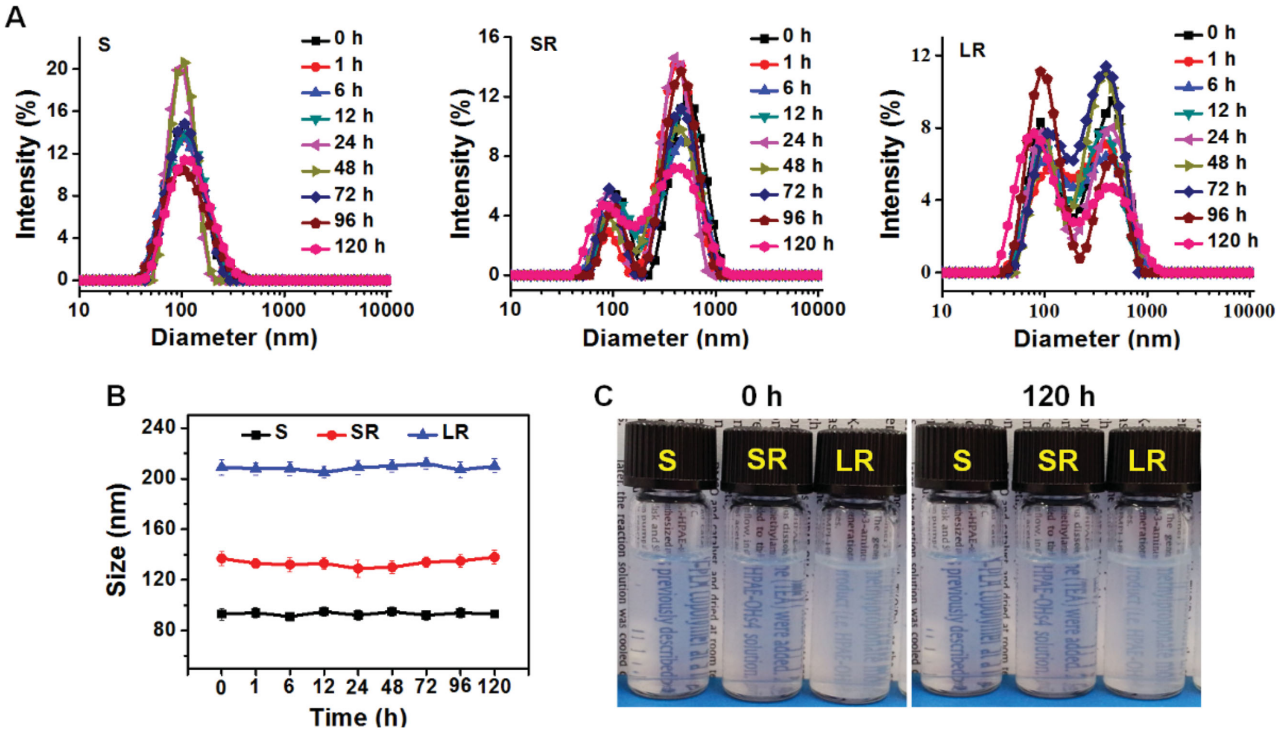

Figure 2. The stability of the spherical (S), short rod (SR), and long rod (LR) micelles at a concentration of 1 mg mL^{-1} in 0.9% physiological saline solution as a function of time. A) Size distribution. B) Average size changes of the micelles over time. The data are shown as the mean ± standard deviation (SD) ($n = 3$). C) Photographs of the micelle solution at 0 and 120 h.

solution. Therefore, these micelles could be stably dispersed in fluid for further utilization in cell culture and animal experiments.

The DOX loading contents (LC) and encapsulation efficiencies (EE) are listed in Table S1 (Supporting Information). The loading capacity of DOX in the LR micelles (EE: 92.3 ± 4.94%) was the highest among all of the tested micelles. The release behaviors of DOX of the micelles with diverse morphologies were assessed in phosphate buffer solution (PBS) at pH 7.4 and acetate buffer solution (ABS) at pH 5.0, which were used to simulate the physiologically neutral condition and the acidic tumor microenvironment, respectively. As shown in **Figure 3**A, an apparent biphasic release profile was observed for all drug-loaded micelles at both pH 7.4 and 5.0. All micelle formulations demonstrated an initial burst release over the first 6 h, followed by an extended release over a prolonged period of time. S@DOX, SR@DOX, and LR@DOX were considerably stable at pH 7.4, and each respective formulation released approximately 38.42 ± 2.68%, 42.15 ± 1.06%, and 47.08 ± 1.45% of cumulative DOX over 72 h. At pH 5.0, the cumulative release was significantly increased, reaching 74.86 ± 2.67% for S@DOX, 79.70 ± 3.58% for SR@DOX, and 84.50 ± 3.88% for LR@DOX. The much faster DOX release profile at pH 5.0 was presumably due to the protonation of the glycosidic amine groups of DOX under acidic conditions.[46,47]

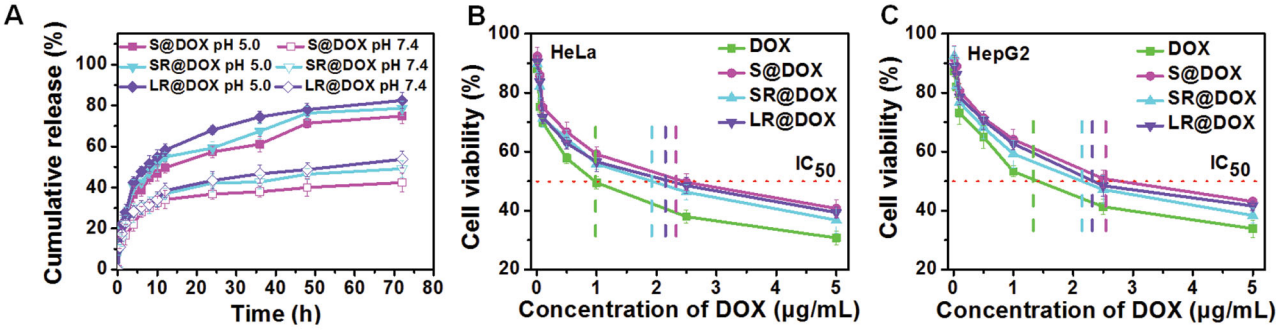

Figure 3. In vitro release and cytotoxicity. A) DOX release from S@DOX, SR@DOX, and LR@DOX micelles in PBS (pH 7.4) and ABS (pH 5.0) at 37 °C. B,C) Cytotoxicity of HeLa cells and HepG2 cells treated with free DOX and S@DOX, SR@DOX, or LR@DOX micelles as a function of DOX concentration. The values represent the mean ± SD ($n = 3$).

2.3. In Vitro Cytotoxicity and Cell Apoptosis

Figure 4A shows the viability of the HeLa, HepG2, and OB cells after treatment with different concentrations (25–500 μg mL^{-1}) of S, SR, and LR blank micelles. The results indicated that more than 90% of the cells remained viable. The corresponding fluorescent images from live cell staining (Figure 4B) showed that each group of cells had good growth and morphology, suggesting that all these micelles possessed good cytocompatibility.

To further compare the influence of shape on the behavior of the micelles, the in vitro antitumor efficiency of free DOX, S@DOX, SR@DOX, and LR@DOX micelles was evaluated in HeLa and HepG2 cells for 48 h (Figure 3B,C). It is worth noting that the IC_{50} values for free DOX, S@DOX, SR@DOX, and LR@DOX were 1.01, 2.49, 1.96, and 2.24 μg mL^{-1} in HeLa cells, respectively, which were slightly lower than the respective IC_{50} values of 1.42, 2.85, 2.17, and 2.36 μg mL^{-1} in HepG2 cells. The cell resistance to DOX is associated with the cell type.[19,48] The micelle morphology is of paramount importance for the differences in the IC_{50} values, presumably because differently shaped micelles have different DOX loading capacities as well as different cellular uptake efficiencies.

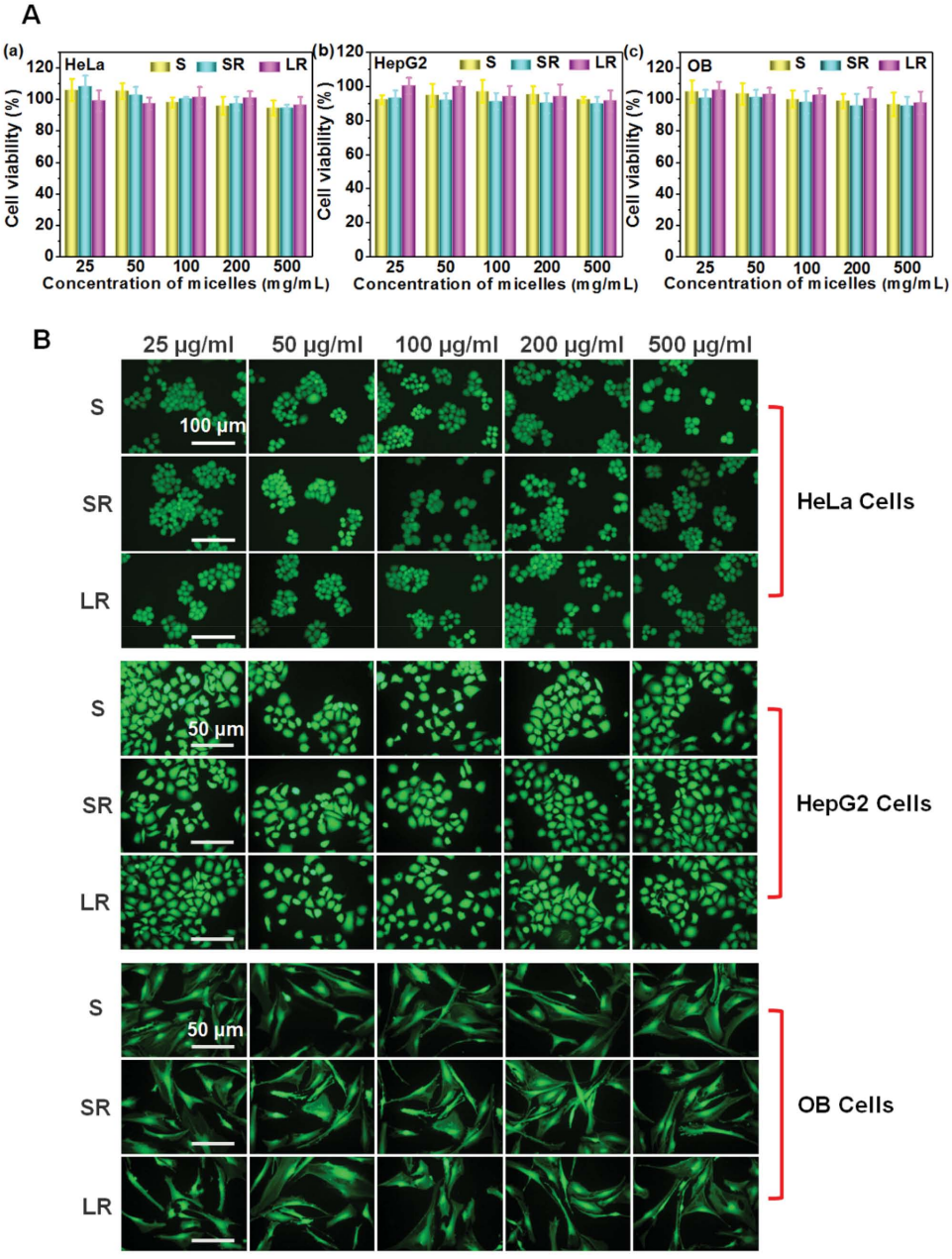

Figure 4. A) Cell survival of S, SR, and LR blank micelles with different concentrations against a) HeLa cells, b) HepG2 cells, and c) OB cells incubated for 24 h. Data are shown as mean ± SD (n = 3). B) Fluorescence images of HeLa cells, HepG2 cells, and OB cells. Green calcein fluorescence indicating live cells.

To investigate whether the cytotoxicity was mediated by DOX-induced cell apoptosis, the Annexin V-FITC Apoptosis Detection kit was used to stain the HeLa or HepG2 cells after incubation with the various DOX-loaded formulations. The apoptotic cells were subsequently monitored by flow cytometry. Annexin V is a Ca^{2+}-dependent phospholipid-binding protein with high affinity for phosphatidylserine, which is translocated from the inside to the outside of lipid membranes during cell apoptosis. FITC-labeled Annexin V was used as a fluorescent probe to detect cell apoptosis. Propidine iodide (PI) is a type of nucleic acid dye that can permeate the plasma membrane of necrotic and middle-to-late-stage apoptotic cells and stain their nuclei. The synergistic effects of Annexin V and PI can distinguish between the different stages of apoptosis. Cells maintained in PBS were used as the negative control. The percentages of necrotic (upper left quadrant), early apoptotic (lower right quadrant), late apoptotic (upper right quadrant), and total dead cells shown in **Figure 5**A were plotted as a histogram in Figure 5B. Specifically, the control group showed negligible apoptotic and necrotic cells in both the HeLa and HepG2 cell lines. After the HeLa cells were treated for 24 h with the DOX-loaded micelles, S@DOX induced 28.7% cell apoptosis and 5.2% cell necrosis; LR@DOX induced 37.6% cell apoptosis and 9.3% necrosis; and SR@DOX induced 38.4% apoptosis cell and 9.8% cell necrosis. By comparison, the total cell death of HepG2 cells was 46% in the SR@DOX group, which slightly higher than the 43.6% cell death in the LR@DOX group. These results indicate that the morphology of the micelles could affect the apoptosis of both HeLa and HepG2 cells. These flow cytometry results showing the cell apoptosis were also in line with the in vitro antitumor efficiencies evaluated using the Alamar blue assay.

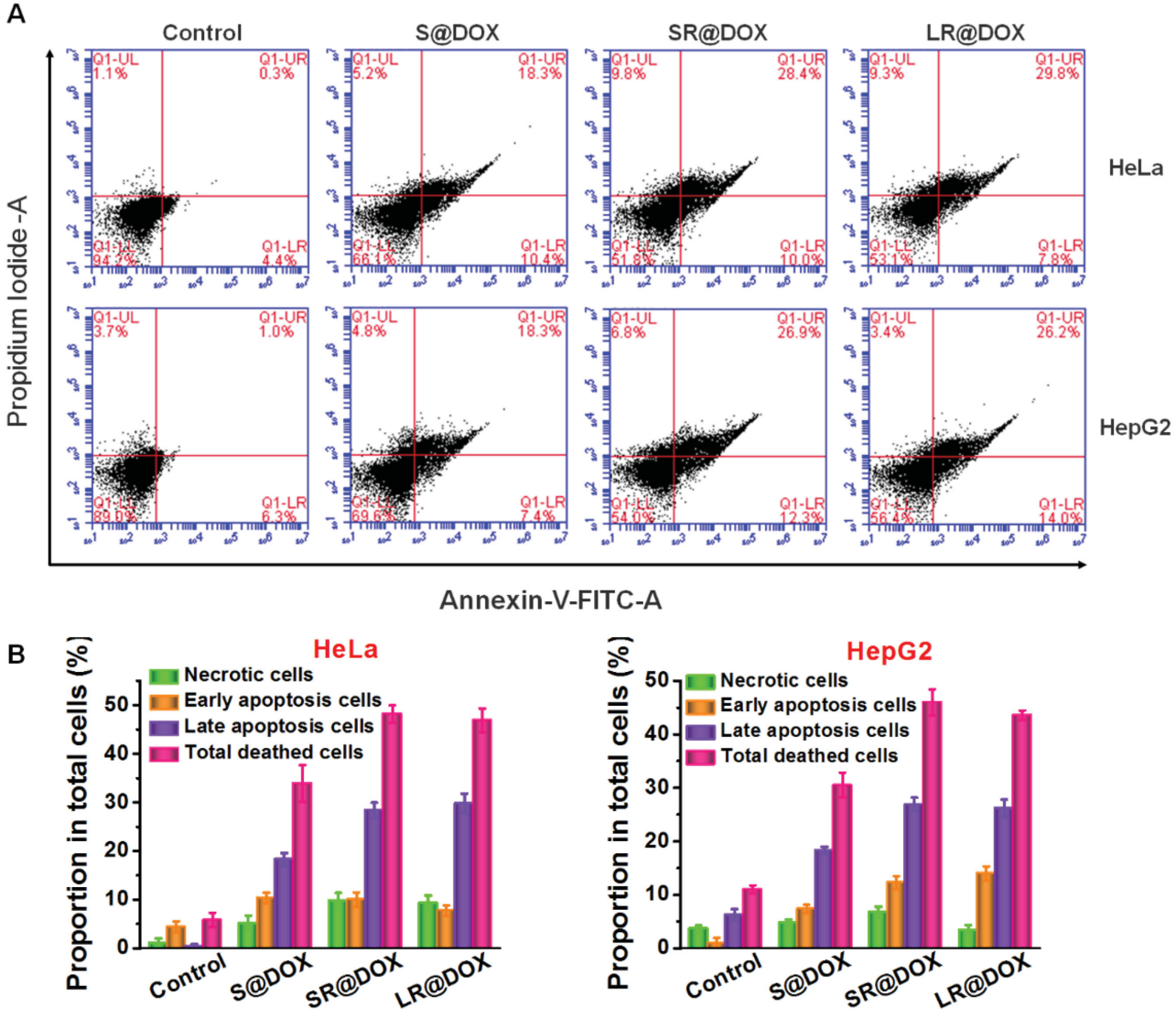

Figure 5. Evaluation of apoptosis in HeLa cells and HepG2 cells treated with PBS (control), S@DOX, SR@DOX, and LR@DOX. A) The cells were treated with an equivalent DOX dose of 5 μg mL^{-1} after 24 h incubation, dual-stained with FITC-conjugated Annexin V (horizontal axis) and propidium iodide (vertical axis) and analyzed using flow cytometry. B) Quantitative analysis of HeLa and HepG2 cell apoptosis ($n = 3$).

2.4. The Effect of Micellar Shape on Cellular Uptake Efficiency and Internalization Pathways

To evaluate the effects of the micellar shape on the cellular uptake efficiency, the HeLa and HepG2 cells were cultured with the S@DOX, SR@DOX, and LR@DOX micelles. The kinetics of cellular uptake were first evaluated by fluorescence microscope analysis, and we found that the intracellular fluorescent intensity increased gradually as the culturing time increasing from 0.5 to 6 h. This finding was in agreement with a prior study, which reported that the cellular uptake of drug-loaded micelles is time-dependent.[49] Meanwhile, confocal laser scanning microscopy (CLSM) and flow cytometry were employed to observe and quantify the intracellular distribution of the micelles after 3 h of incubation. In the CLSM images (**Figure 6**A1,A2), SR@DOX exhibited the highest fluorescence intensity, followed by LR@DOX, and finally by S@DOX. These observations were further verified using flow cytometry (Figure 6B1,B2). The bio-inspired, rod-like micelles had relatively high uptake efficiencies in comparison to spherical micelles. One possible explanation is that rod-shaped micelles have multivalent interactions with the cell membranes, resulting in stronger adhesions and more sites for the uptake of the micelles relative to spheres, which theoretically have only one contact point with a single cell.[16,50,51]

The cellular internalization and intracellular distribution of the micelles were further investigated to obtain a detailed visualization. The ultrathin section samples of the HeLa cells cultured with S, SR, and LR micelles for 6 h were observed using TEM, as shown in Figure 6C. All of the micelles could be internalized by the cells and were found within the red-dotted line circles in the TEM images. As predicted, the micelles were encapsulated into vesicles or were dispersed in the cytoplasm. Additionally, the integrated and normal cellular structures were seen in all the micelle-treated cells, which further verified the outstanding cytocompatibility of these micelles.

To determine whether polymer micelles with different morphologies are internalized via different pathways, we explored the uptake of polymer micelles by HeLa and HepG2 cells. Three types of inhibitors, namely chlorpromazine (CPZ), genistein

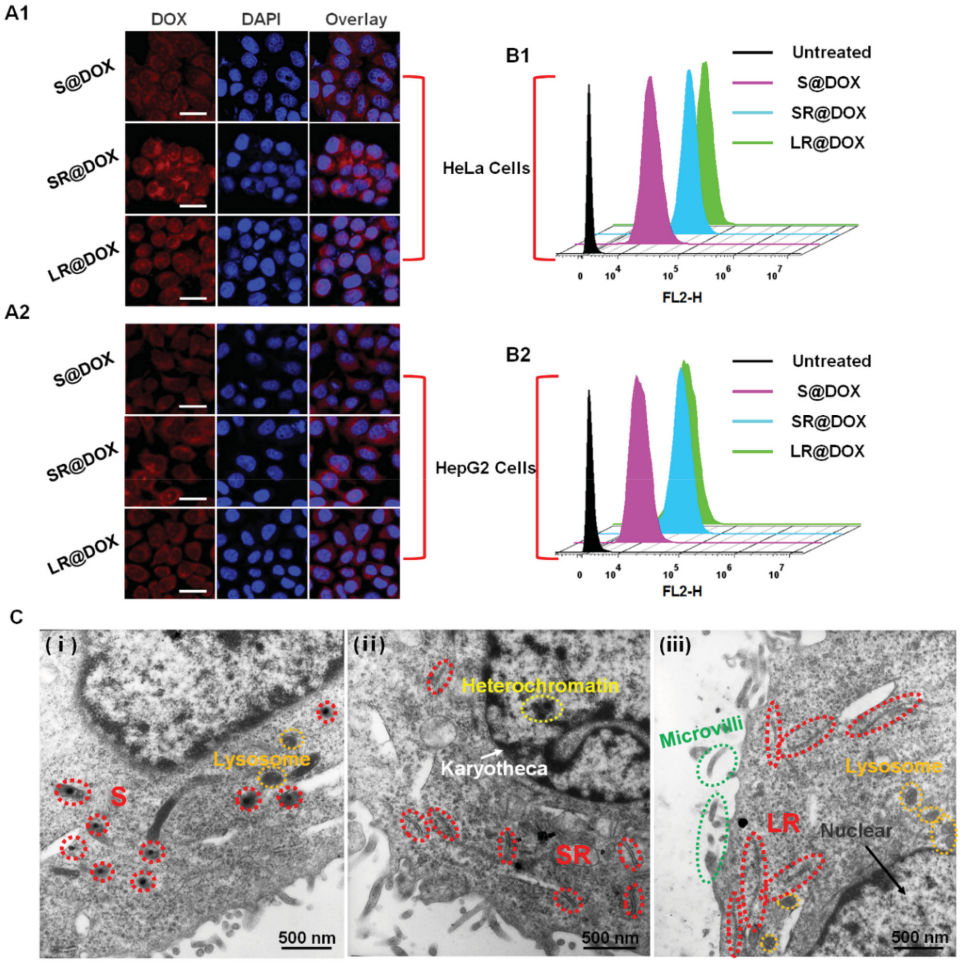

Figure 6. Cellular internalization. A1,A2) CLSM images of HeLa cells and HepG2 cells incubated with S@DOX, SR@DOX, and LR@DOX micelles (red) for 3 h. The cell nuclei were stained with DAPI (blue) and the scale bars are 20 μm. B1,B2) Flow cytometry histograms of HeLa cells and HepG2 cells treated with S@DOX, SR@DOX, and LR@DOX or without treatment (control) for 3 h at 37 °C. DOX-equivalent dose: 5 μg mL^{-1}. C) High-resolution TEM images of ultrathin section of Hela cells after 6 h incubation with (i) spherical (S), (ii) short rod-like (SR), and (iii) long rod-like (LR) micelles. The internalized micelles are shown in the red dotted line circles. The scale bars are 0.5 μm.

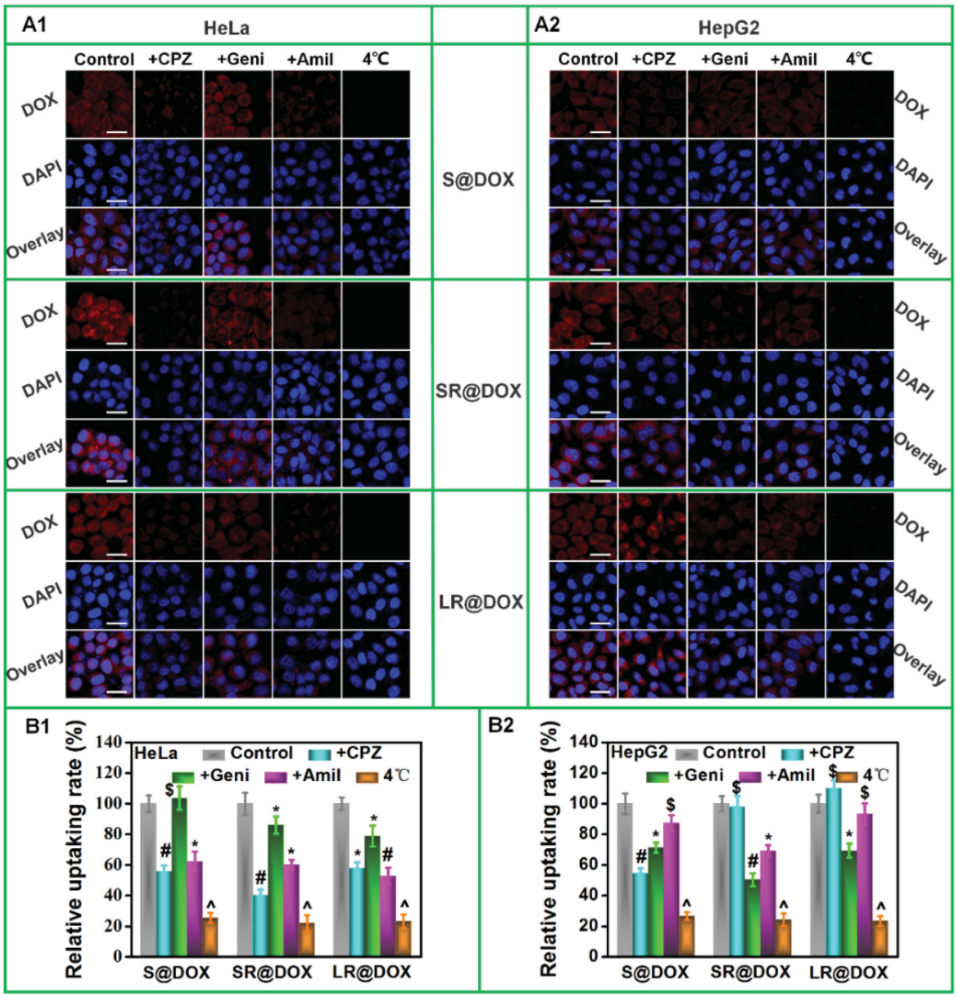

Figure 7. Evaluation of the endocytic pathways of S@DOX, SR@DOX, and LR@DOX micelles in Hela and HepG2 cells. A1,A2) CLSM images showing cells incubated at 4 °C with different endocytic inhibitors: none (Control); chlorpromazine (+CPZ, 10 μg mL^{-1}); genistein (+Geni, 50 μg mL^{-1}); and amiloride (+Amil, 13.3 μg mL^{-1}). The nuclei were stained with DAPI (blue). The DOX dosage was 5 μg mL^{-1}. The scale bars are 20 μm. B1,B2) Quantitative analysis of HeLa and HepG2 cells obtained by the Image-Pro Plus 6.0 software. The data are represented as the mean ± SD ($n = 3$). $, not significant; *, $P < 0.05$; #, $P < 0.01$; and ^, $P < 0.001$ compared to the Control in the same sample group (one-way ANOVA using Excel 2013).

(Geni), and amiloride (Amil), were chosen to block clathrin-mediated endocytosis,[50,51] caveolae-mediated endocytosis,[52,53] and macropinocytosis,[52] respectively. Low temperatures (4 °C) were used to show that the cellular uptake of micelles is an active, energy-intensive process.[53] The inhibitor concentrations and acting time were optimized according to the results of other publications in order to achieve a minimum of 90% cell viability.[50,51] The CLSM images of HeLa and HepG2 cells pretreated with inhibitors are shown in **Figure 7**A1,A2. The relative uptake rates were acquired from these images using Image-Pro Plus 6.0 (Figure 7B1,B2) and flow cytometry results in Figure S4 (Supporting Information). Drastic decreases in the uptake of these micelles by both of these cell types were observed at 4 °C under the pretreated conditions (an almost 80% reduction in all types), suggesting that the endocytosis of micelles with different morphologies was indeed an energy-dependent process. The uptake of all micelles by HeLa cells primarily occurred via the clathrin-mediated endocytosis and micropinocytosis pathways. By contrast, the role of caveolae-mediated endocytosis could not be ignored for the uptake of SR@DOX and LR@DOX. The cellular internalization of the rod-shaped micelles via all of the internalization pathways may be the reason that more rod-shaped micelles than spherical micelles were internalized.[25] Nevertheless, in HepG2 cells, the caveolae-mediated endocytosis was found to be the primary uptake pathway for all the micelles, though S@DOX was internalized mainly through clathrin-mediated endocytosis. Therefore, we concluded that the cellular internalization mechanism varied significantly according to both the micelle geometry and the cell type. Moreover, the internalization of micelles of various shapes appears to be mediated by multiple pathways.[20,25,52]

2.5. In Vivo Pharmacokinetics and Biodistribution

The shape-dependent in vivo blood circulation and tissue distribution of the different DOX formulations were studied after a single i.v. injection of each formulation into H22-tumor-bearing

Balb/c mice. The DOX concentrations in the collected plasma and tissues (heart, liver, spleen, lung, kidney, and tumor) at certain time intervals were determined using fluorescence spectroscopy. The pharmacokinetic profiles of free DOX, S@DOX, SR@DOX, and LR@DOX are shown in **Figure 8**A,B. From the blood clearance curves (Figure 8A), we found that the LR@DOX was eliminated significantly more slowly than the other formulations, and there was still 30.43 ± 2.96% of the injected dose after 24 h. In contrast, after 6 h, free DOX was barely detected in the blood. The relevant pharmacokinetic parameters were calculated by fitting the blood DOX concentration versus time in a two-compartment model using PKSolver (Figure 8B). The elimination half-life ($t_{1/2\beta}$) of LR@DOX (24.23 ± 2.87 h) was remarkably higher than that of SR@DOX (14.30 ± 1.62 h), S@DOX (8.39 ± 0.53 h), and free DOX (1.34 ± 0.24 h). In addition, the area under the curve (AUC) for the LR@DOX (947.46 ± 82.65 μg mL^{-1} × h) was much higher than the AUC values for SR@DOX (431.74 ± 45.05 μg mL^{-1} × h), S@DOX (70.90 ± 9.60 μg mL^{-1} × h), and free DOX (20.88 ± 1.24 μg mL^{-1} × h). By further comparison with free DOX, S@DOX, SR@DOX, and LR@DOX showed significantly higher values for mean retention time (MRT; 2.92-, 5.30-, and 9.10-fold increases, respectively), and lower body clearance (CL) of DOX (5-, 17-, and 31-fold decreases, respectively). In short, these results suggested that all of the micellar DOX formulations prolonged the blood circulation of DOX though LR@DOX in particular possessed the longest circulation.[54,55]

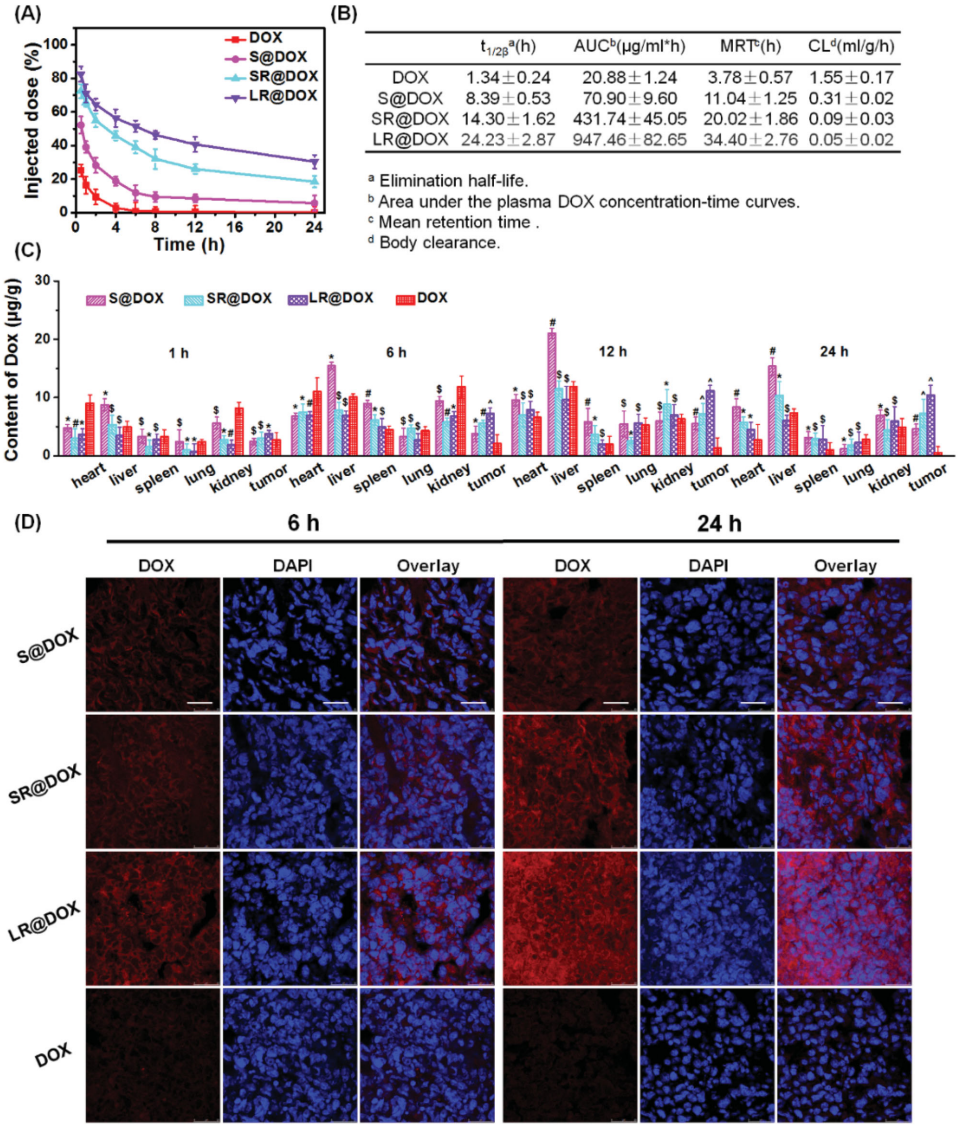

	$t_{1/2\beta}$[a](h)	AUC[b](μg/ml*h)	MRT[c](h)	CL[d](ml/g/h)
DOX	1.34±0.24	20.88±1.24	3.78±0.57	1.55±0.17
S@DOX	8.39±0.53	70.90±9.60	11.04±1.25	0.31±0.02
SR@DOX	14.30±1.62	431.74±45.05	20.02±1.86	0.09±0.03
LR@DOX	24.23±2.87	947.46±82.65	34.40±2.76	0.05±0.02

[a] Elimination half-life.
[b] Area under the plasma DOX concentration-time curves.
[c] Mean retention time .
[d] Body clearance.

Figure 8. In vivo pharmacokinetics and biodistribution. A) Pharmacokinetic profiles of total DOX after tail vein injection of various DOX formulations (dose: 2 mg DOX per kg body weight) (n = 3). B) Pharmacokinetic parameters of various DOX formulations. C) Biodistribution of DOX in different tissues after intravenous injection of various formulations at a dosage of 2 mg kg^{-1} (n = 3). $, not significant; *, $P < 0.05$; #, $P < 0.01$; ^, $P < 0.001$, compared with free DOX at the same time point. D) The representative CLSM images of the tumor cryo-sections from H22 tumor-bearing mice after intravenous administration of S@DOX, SR@DOX, LR@DOX micelles, and free DOX at an equivalent DOX dose of 2 mg kg^{-1} at 6 and 24 h. The scale bars represent 25 μm. The blue coloring represents cell nuclei.

The in vivo biodistributions of the diversely shaped micelles were measured in a time-dependent manner (1, 6, 12, and 24 h after i.v. administration) (Figure 8C). At the examined time, the accumulation of DOX in tumors after delivery via the S@DOX, SR@DOX, and LR@DOX micelles were all significantly enhanced in comparison to free DOX at 6, 12, and 24 h. These increases were 7.84-, 12.59-, and 17.98-fold higher at 24 h for S@DOX, SR@DOX, and LR@DOX relative to free DOX. Furthermore, the DOX content of the free DOX group decreased in tumors over time, while the levels of DOX released from all micelles continuously increased in tumor tissues except at 24 h, when the levels were slightly lower than those at 12 h. The high accumulation of the drug in the tumors was primarily due to two main reasons: first, the blood circulation time was enhanced due to the ability of the micelles to evade specific recognition by the reticuloendothelial system (RES) due to the PEGylation of the micellar outer shell and their flexible, elongated shapes; second, the uptake of the micelles was mediated by the EPR effect.[56] The accumulation of S@DOX in the liver was ≈1.48 times greater than the accumulation of SR@DOX and 2.52 times greater than that of LR@DOX. A similar trend was found in the spleens, which indicated that the RES more favorably cleared the spherical micelles than the rod-like micelles.[28,57,58] Furthermore, the CLSM analysis of the tumor cryo-sections 6 and 24 h after injection is shown in Figure 8D. The highest fluorescence intensity was also found in the LR@DOX group at 6 h, especially at 24 h, indicating the strongest accumulation in tumor tissues.

2.6. In Vivo Antitumor Effect and Histological Analysis

To further evaluate the influence of micellar morphology on the in vivo antitumor effects, the DOX-loaded micelles with various shapes were injected into Balb/c mice bearing H22 tumor xenografts. As shown in **Figure 9**A, the changes in body weights as a function of time were taken to be the safety profiles of the various formulations. Compared with the initial body weights, all of the groups except for the free DOX exhibited a modest increase over the 21 d of evaluation, indicating that no significant systemic toxicity was noticed in either the control or drug-loaded groups. The tumor volumes and tumor weights were monitored and characterized as the parameters of the cancer therapeutic effects. Based on the tumor volumes (Figure 9B,D), all the DOX-loaded micelles showed pronounced inhibitory effects on tumor growth compared with the 0.9% saline solution and blank micelles groups. This was especially the case for LR@DOX, which exhibited the most distinct suppressive effects. The tumor volume of the saline group expanded rapidly from 25.08 ± 1.85 to 1281.49 ± 81.2 mm^3 within 21 d. The S, SR, and LR blank micelles showed similar growth profiles, reaching 955.31 ± 87.45 (S), 979.96 ± 69.46 (SR), and 1135.19 ± 73.58 mm^3 (LR). These results indicated that the blank micelles barely had any physiological activities. By contrast, those groups treated with S@DOX, SR@DOX, and LR@DOX showed severe reductions in tumor volume, which decreased to 475.26 ± 77.83, 336.56 ± 56.59, and 292.34 ± 93.02 mm^3, respectively. These tumors were significantly smaller than those of the saline-treated mice and the groups treated with each type of blank micelles. The inhibition rate (IR) of tumor growth was calculated on the basis of the tumor volume on the 21st day. The IR of the LR@DOX micelles was 80.15% ± 2.54%, which represented a 1.07-, 1.25-, and 1.46-fold increase relative to SR@DOX, S@DOX, and free DOX, respectively. As shown in Figure 9C, the tumor weight was 0.9058 ± 0.097 g in the saline group on the 21st day, which was almost 3.53 times heavier than that of the LR@DOX group. From the data shown in Figures 6, 7, 8, we knew that the LR@DOX had a significant cellular uptake by tumor cells and rapidly released their payloads in the acidic tumor microenvironment, subsequently leading to the marked levels of cancer cell death.

To further confirm the therapeutic efficacies of the DOX-loaded micelles, immunohistochemical studies of tumor sections were performed on the 10th and 21st days after the first injection. Figure 9E shows the TdT-mediated dUTP nick end labeling (TUNEL)-stained images in which the pale yellow or dark brown represents necrotic areas or apoptotic cells. In comparison with the saline and blank micelle groups on both the 10th and 21st days, the free DOX, S@DOX, SR@DOX, and LR@DOX groups exhibited distinct degrees of apoptosis: the nuclei were narrower, the nuclear membranes were shrunken, and the chromatin was condensed. These indicators of apoptosis were most obvious in the LR@DOX group, which supported the excellent therapeutic effect of these micelles. Furthermore, the apoptotic rate was evaluated in Image-Pro Plus 6.0 using the results of the TUNEL analysis (Figure 9F). The LR@DOX also presented the highest apoptotic rate (86.3 ± 2.03%), which was consistent with the reduced tumor growth rates that were calculated from the tumor volumes and indicated that the LR@DOX micelles had superior antitumor effects compared to the other formulations. Additionally, the expression of endothelial cells was measured by immunohistochemical staining of CD31 to evaluate the suppression of angiogenesis. The light yellow or tan color in the images represents the positive expression of the CD31 antibody. As shown in Figure S5 (Supporting Information), the immunoreactive microvessels in mice treated with free DOX, S@DOX, SR@DOX, or LR@DOX were clearly decreased or disrupted in comparison to those observed in the groups treated with saline or blank micelles. The cells dissolved and the nuclei were seriously fragmented, and severe inflammatory responses developed in all groups treated with the DOX-loaded formulations. This was especially the case for LR@DOX. In conclusion, DOX-loaded micelles with long, rod-like shapes have the highest anticancer function.

3. Conclusion

In summary, as a proof of concept, we developed an original bio-inspired rod-shaped polymer micellar system similar to the structures of bacterial pathogens by simply adding NaCl salt to the aqueous solution in the micelle self-assembly process. Compared with the sphere-shaped micelles, the rod-like micelles represented the greatest drug-loading efficiency, the fastest drug-release behavior in a simulated tumor acidic microenvironment, and the highest internalization rate by tumor cells. The in vivo experimental results demonstrated that the rod-shaped micelles had a great capacity of overcoming the rapid clearance of RES with a long circulation in blood (the elimination half-life

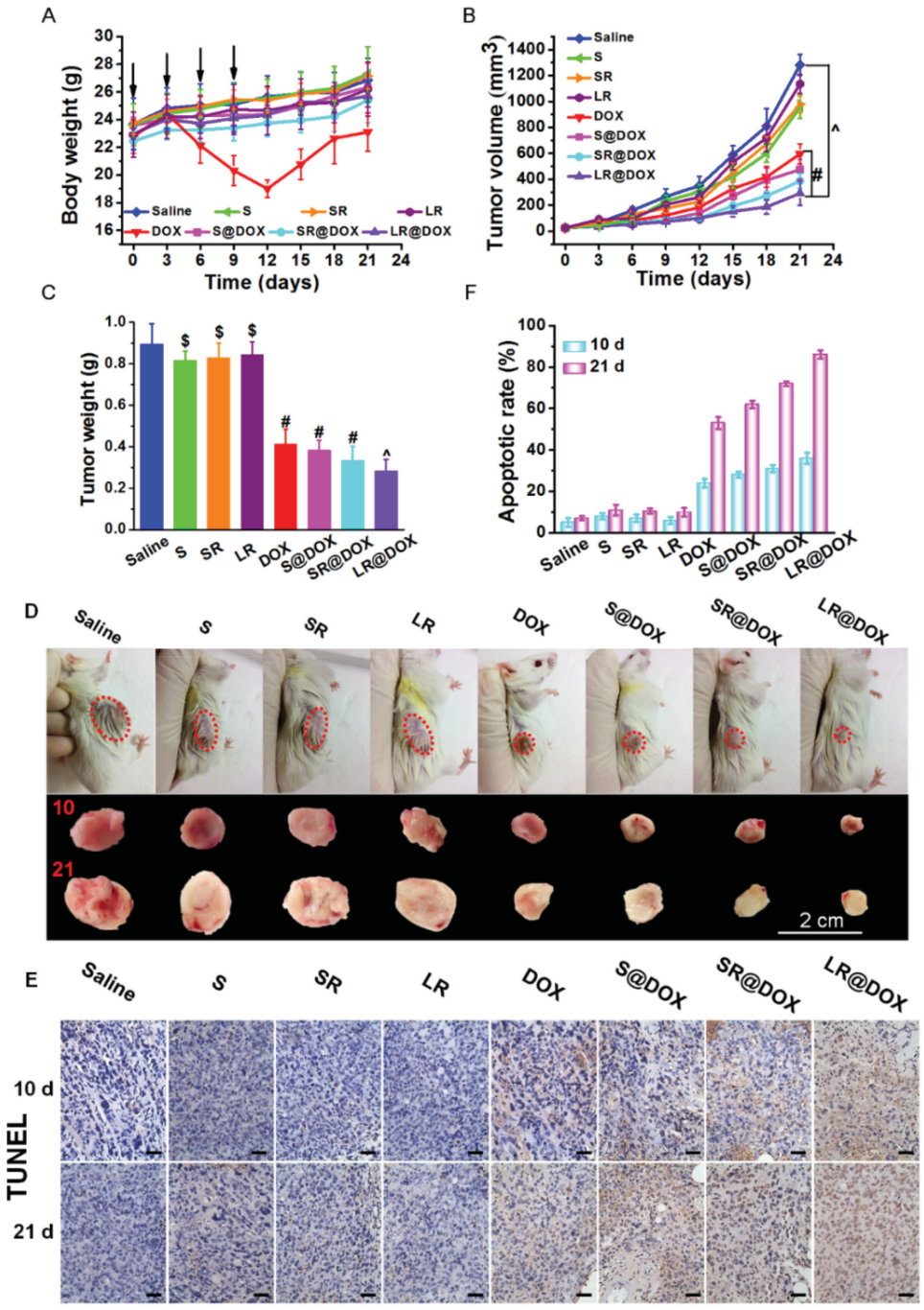

Figure 9. In vivo antitumor activity evaluation. H22 tumor-bearing Balb/c mice are treated with free DOX S@DOX, SR@DOX, and LR@DOX micelles at a dose of 2 mg kg^{-1} ($n = 5$). A) Body weight change. B) Tumor volume change. C) Excised tumor weight at the 21st day. D) Tumor-bearing H22 mice at the 21st day and excised solid tumors at the 10th and 21st days. E) TUNEL analysis of the tumor sections at 10th and 21st day after the first treatment (scale bars = 200 μm). F) The apoptotic rate of tumor sections calculated in the TUNEL analysis using Image-Pro Plus 6.0. The data in (A), (B), (C), and (F) are the mean ± SD; $, not significant; *, $P < 0.05$; #, $P < 0.01$; and ^, $P < 0.001$ compared with the saline group.

is ≈18-fold longer than that of free drugs), a high rate of accumulation in tumor tissues, and a significant enhancement of the therapeutic agent potency against artificial solid tumors. These findings demonstrated that the bio-inspired rod-shaped nanoplatform has great potential in the development of advanced drug-delivery systems for enhanced cancer therapy.

4. Experimental Section

Morphology Optimization of Micelles: Monomethoxy poly(ethylene glycol)-*block*-poly(ε-caprolactone) (mPEG-CL_{41}) copolymer with mPEG/CL weight ratio of 3:7 (M_n 7500 Da and PDI 1.65 obtained by GPC measurements) was synthesized according to a previous report.[59,60] The micelles were fabricated using the solvent evaporation method. Briefly,

10 mg of mPEG-CL_{41} dry powder was dissolved in 5 mL tetrahydrofuran (THF) as a good solvent in a 50 mL beaker. Then, 10 mL deionized water was added dropwise using a glass syringe (10 mL gauge) under high-speed stirring into the beaker. The mixed solution was stirred on medium–low speed at room temperature to remove the THF completely to yield the micelles.

For the mPEG-CL_{41} micelles with different morphologies, the fabrication process was similar to that mentioned above, but sodium chloride (NaCl) was added to the aqueous solution at different concentrations. Concentrations of 0, 0.03, 0.05, 0.08, 0.1, 0.13, 0.15, and 0.2 M NaCl in solution were investigated in the optimization of the micellar shapes. When the THF was completely volatilized, the micelles with various morphologies were yielded. Among all of the morphologies, three main types of nanostructures, including S (at 0 M NaCl), SR (at 0.05 M NaCl), and LR (at 0.1 M NaCl), were investigated in parallel in the subsequent drug-loading and release tests, in vitro assays, and in vivo analyses described in the later sections. The anticancer drug DOX·HCl was dehydrochlorinated and was used as a model anticancer drug for fabricating DOX-loaded micelles with different morphologies (named as S@DOX, SR@DOX, and LR@DOX according to the shapes of the micelles). The procedure was almost identical to that described above, except that DOX was dissolved along with the copolymer in THF and the final micelle solution was transferred into a dialysis bag (MWCO 1000) and dialyzed against deionized water several times to remove the free DOX.

Characterization: AFM (CSPM5000, Bejing, China) was employed to observe the morphologies of the micelles. Tapping mode with the scan frequency of 5 Hz was used to observe the morphology of micelles. TEM studies were performed with a JEOL 2100F instrument (JEOL Ltd., Japan) operated at a voltage of 200 kV to further observe the micelles morphology. The micelles loading with Nile red as fluorescence probe were viewing directly by a Leica TCS SP5 confocal laser scanning microscope. DLS was performed using a Malvern Zeta-sizer Nano-ZS90 (Malvern, UK) to determine the mean size and size distribution of the micelles at room temperature.

In Vitro Drug Release: DOX was selected as an anticancer drug model to determine the loading and release profiles. The drug LC and EE were measured using a UV–vis spectrophotometer (UV-2550, Shimadzu, Japan). The lyophilized micelle powder of S@DOX, SR@DOX, and LR@DOX was weighed and dissolved in DMSO and the absorption was measured by UV at 488 nm to quantify the concentration of DOX using a pre-established DOX calibration curve. The in vitro release kinetics of DOX from the differently shaped micelles were investigated in PBS at pH 7.4 and ABS at pH 5.0 using dialysis bags with a molecular weight cutoff of 1000 g mol^{-1}. The amounts of DOX released from S@DOX, SR@DOX, and LR@DOX were determined using a fluorescence spectrophotometer (F-7000, Hitachi, Japan).

In Vitro Cytotoxicity Assay: HeLa, HepG2, and OB cells were seeded into 48-well plates at a density of 1.0×10^4 cells per well and were supplemented with RPMI 1640 or α-MEM medium containing 10% newborn calf serum. The plates were maintained at 37 °C in a humidified atmosphere containing 5% CO_2 for 24 h. Subsequently, the cells were treated with S, SR, and LR in separate treatment groups at concentrations ranging from 25 to 500 μg mL^{-1} prior to incubation for another 24 h. The medium was carefully removed 24 h later and the cells were rinsed with PBS. Thereafter, 300 μL Alamar blue solution (10% Alamar blue, 80% media 199 (Gibcos), and 10% FBS; V/V) was added into each well, and the plates were incubated for another 4 h. Next, 200 μL of the reduced Alamar blue solution was pipetted into 96-well plates, and the absorbance was read in an automated microplate spectrophotometer (ELX800 Biotek, USA) at 570 nm (excitation)/600 nm (emission). The results are the mean ± standard deviation (SD) in triplicate. For the live cell staining, HeLa cells, HepG2 cells, or OB cells were treated with S, SR, and LR blank micelles at different concentrations ranging from 25 to 500 μg mL^{-1}. The treated cells were incubated for 24 h, washed with PBS, and supplemented with 2×10^{-6} M of calcein acetoxymethylester (Calcein-AM) staining solution, and incubated for 10 min. The live cells were stained green when visualized by FM.

To evaluate the in vitro antitumor activity of S@DOX, SR@DOX, LR@DOX micelles, and free DOX, we performed a tumor cell inhibition test on HeLa and HepG2 cells using the Alamar blue assay. In brief, HeLa or HepG2 cells were plated at a density of 1×10^4 in a 48-well plate and incubated for 24 h in a humidified condition with 5% CO_2 at 37 °C. Afterward, free DOX and DOX-loaded micelles with DOX dosages varying from 0.01 to 5 μg mL^{-1} were added to the plates, and the cells were incubated for 48 h. The cell viabilities were determined using the Alamar blue assay mentioned above. To quantitatively measure the apoptosis of cancer cells affected by differently shaped micelles, HeLa cells and HepG2 cells were seeded into 6-well culture plates at a density of 2×10^5 cells per well and incubated at 37 °C in a 5% CO_2-humidified atmosphere for 24 h. The apoptosis of cells exposed for 24 h to the DOX-loaded micelles at a DOX concentration of 5 μg mL^{-1} was determined by flow cytometry (FCM) (BD Accuri C6, USA). After treatment, the cells were trypsinized with EDTA-free trypsin, centrifuged at 2000 rpm for 5 min, washed twice with cold PBS, harvested in binding buffer, and stained with Annexin V-FITC and propidium iodide in accordance with the manufacturer's protocol.

In Vitro Cellular Uptake Analysis: The in vitro cellular uptake of the differently shaped DOX-loaded micelles was investigated in HeLa and HepG2 cells with FM, CLSM, and FCM. For FM observation, HeLa and HepG2 cells were separately seeded into 6-well plates at a density of 1.0×10^5 cells per well with 2 mL RPMI 1640 media for 24 h. The S@DOX, SR@DOX, and LR@DOX micelle solutions (each containing 5 μg mL^{-1} of DOX) were added into separate wells, and the plates were incubated for 0.5, 1, 3, and 6 h. Next, the medium was removed, and the cells were washed three times with PBS. The cells were then fixed with 2 mL 2.5% glutaraldehyde for 30 min, and the cell nuclei were stained with 4′,6-diamidino-2-phenylindole (DAPI, blue) for 7 min. For CLSM (FV1000, Olympus, Japan) viewing, the procedure was almost similar to that described for FM observation. The difference is that the culture time is only 3 h. The FCM analysis is also similar with FM observation. The difference is that after 3 h incubation with S@DOX, SR@DOX, and LR@DOX, the cells were washed three times with PBS and were detached using the EDTA-containing trypsin solution. The cells were then centrifuged at 2000 rpm for 3 min and resuspended in PBS. Finally, 2.0×10^4 cells were gated and analyzed by FCM, and the quantitative results were acquired using the FlowJo software. The uptake of S, SR, and LR micelles was observed by ultrathin section TEM. The HeLa cells were cultured with 0.5 mg mL^{-1} S, SR, or LR for 6 h at 37 °C. After the treatment, the cells were washed three times with PBS, collected by centrifugation, and prefixed with 0.5% glutaric dialdehyde for 10 min at 4 °C. The cells were then centrifuged at 13 000 rpm for another 15 min, harvested in a 1.5 mL EP tube, postfixed with 3% glutaric dialdehyde, and stored at 4 °C. The ultrathin section samples were observed by TEM (HITACHI, H-600IV, Japan).

HeLa and HepG2 cells (2.0×10^5 cells per well) were separately seeded in 6-well plates with 2 mL RPMI 1640 media and incubated for 24 h. The effects of temperature on the cellular uptake of micelles were studied by preincubating the cells at 4 °C for 3 h. S@DOX, SR@DOX, and LR@DOX with DOX dosages of 5 μg mL^{-1} were added to separate wells and were incubated for another 3 h. To evaluate the effect of diverse inhibitors on the cellular uptake of the micelles, the cells were preincubated individually with three different inhibitors of endocytosis for 1 h at 37 °C. The inhibitors selected were CPZ (10 μg mL^{-1}) to inhibit the clathrin-mediated endocytosis, Geni (50 μg mL^{-1}) to inhibit caveolae-mediated endocytosis, and Amil (13.3 μg mL^{-1}) to inhibit micropinocytosis. All inhibitors were used at nontoxic concentrations. Following the pretreatment, S@DOX, SR@DOX, and LR@DOX with DOX dosages of 5 μg mL^{-1} were added, and the plates were incubated for another 3 h. The cells incubated with DOX-loaded micelles without any chemical inhibitor pretreatments were used as the controls. Subsequently, the cells were washed three times with PBS and fixed with 2.5% glutaraldehyde for 30 min, and the cell nuclei were stained with DAPI for 7 min. The fluorescence images were taken using CLSM and the relative uptake rate was calculated using Image-Pro Plus 6.0 software. For quantitative analysis, the cells were washed three times

with PBS and were manipulated in a similar manner to those used in FCM, as described above.

Pharmacokinetics and Biodistribution Studies: H22 tumor xenografts were transplanted into 5-week-old male Balb/c mice. When the tumor volume reached ≈25 mm^3, the mice were randomized into four groups ($n = 3$) and injected intravenously through the tail vein with 2 mg kg^{-1} of free DOX, S@DOX, SR@DOX, or LR@DOX. After administration, blood samples were obtained via eyeball enucleation at selected time intervals (0.5, 1, 2, 4, 6, 8, 12, and 24 h) using a heparinized tube. Plasma samples were harvested by immediately centrifuging the blood samples at 3000 rpm/min for 10 min. The plasma samples were then frozen at −20 °C until analysis. After blood collection at 1, 6, 12, and 24 h, the mice were killed by cervical dislocation of the vertebra, and the normal tissues (including the heart, liver, spleen, lung, and kidney) and the tumor were harvested. The tissues were rinsed in saline, wiped with filter paper, weighed, and homogenized in 1 mL DMSO using a tissue grinder, followed by centrifugation at 3500 rpm for 5 min. The supernatants were collected and frozen at −20 °C for fluorescent analysis. The data were normalized to the tissue weights. The pharmacokinetic parameters such as the elimination half-life ($t_{1/2\beta}$), the AUC, the MRT, and the CL were calculated by fitting the blood concentrations of the pharmaceutical drug versus time to a two-compartment model using PKSolver V2.0. The percent injected dose (% ID) values were calculated as shown in a previous work.[61] For the qualitative evaluation of the drug distribution in the tumor, the mice were sacrificed either 6 or 24 h after drug administration, and the tumors were excised and immediately frozen in liquid nitrogen until further sectioning. The accumulation of DOX in the tumor tissues was visualized by CLSM (FV1000, Olympus, Japan) on frozen, cryo-sectioned 5–7 μm thick tumor tissues.

In Vivo Tumor Inhibition Studies: Balb/c mice bearing H22 tumor xenografts with a volume of ≈25 mm^3 were randomly divided into eight groups ($n = 5$). Various formulations including saline, DOX·HCl, S, SR, LR micelles, and their corresponding DOX-loaded micelles (S@DOX, SR@DOX, and LR@DOX) were injected intravenously through the tail vein into the mice on days 0, 3, 6, and 9. The equivalent DOX dosages of each DOX-loaded formulation were 2 mg kg^{-1}, and a total of 200 μL of each formulation was injected. The body weights of the mice and the tumor volumes were monitored every two days after the first treatment until day 21. The tumor size was measured using a Vernier caliper across its longest (a) and shortest (b) diameters, and the tumor volume (V) was calculated according to the following equation: $V = ab^2/2$. The tumor weights were acquired on the 21st day after the mice were executed, and the excised tumors were weighed. On the 10th and 21st days, some of the mice from each group were sacrificed, and their tumors were isolated and collected in 4% paraformaldehyde for further immunohistochemical staining. The fixed tumor tissues were embedded in paraffin and sectioned into slices at a thickness of 5 μm. The TUNEL and the platelet/endothelial cell adhesion molecule-1 (CD31) antibody were applied to stain the apoptotic cells and microvessels of the tissue sections. The TUNEL and CD31 assays were monitored by optical microscopy at high power (400×) magnifications. The apoptotic rates of the cells were quantitatively described from the TUNEL assay results: three images of each sample were collected for measurement using Image-Pro Plus 6.0, and the results are presented as the average data with SDs. In this study, all animal experiments were approved by the Institutional Animal Care and Use Committee of Sichuan University (P. R. China), and all protocols for this animal study conformed to the Guide for the Care and Use of Laboratory Animals.

Statistical Analysis: For all the experiments, data were expressed as the mean value with SD. Single factorial analysis of variance (ANOVA) was performed to determine statistical significance of the data.

Supporting Information

Supporting Information is available from the Wiley Online Library or from the author.

Acknowledgements

This work was partially supported by the National Basic Research Program of China (973 Program, 2012CB933600) and the National Natural Science Foundation of China (Grant Nos. 30970723, 51173150, 51373138, and 21574105).

Received: August 29, 2015
Revised: October 2, 2015
Published online: November 17, 2015

[1] A. L. Zerda, S. S. Gambhir, *Nat. Nanotechnol.* **2007**, *2*, 745.
[2] D. Peer, J. M. Karp, S. Hong, O. C. Farokhzad, R. Margalit, R. Langer, *Nat. Nanotechnol.* **2007**, *2*, 751.
[3] J. L. Perry, K. P. Herlihy, M. E. Napier, J. M. Desimone, *Acc. Chem. Res.* **2011**, *44*, 990.
[4] A. Albanese, P. S. Tang, W. C. W. Chan, *Annu. Rev. Biomed. Eng.* **2012**, *14*, 1.
[5] M. Dunne, O. I. Corrigan, Z. Ramtoola, *Biomaterials* **2000**, *21*, 1659.
[6] J. Panyam, V. Labhasetwar, *Adv. Drug Delivery Rev.* **2003**, *55*, 329.
[7] H. J. Gao, W. D. Shi, L. B. Freund, *Proc. Natl. Acad. Sci. USA* **2005**, *102*, 9469.
[8] W. Jiang, B. Y. S. Kim, J. T. Rutka, W. C. W. Chan, *Nat. Nanotechnol.* **2008**, *3*, 145.
[9] R. Gref, Y. Minamitake, M. T. Peracchia, V. Trubetskoy, V. Torchilin, R. Lange, *Science* **1994**, *263*, 1600.
[10] S. Stolnik, L. Illum, S. S. Davis, *Adv. Drug Delivery Rev.* **1995**, *16*, 195.
[11] G. Storm, S. O. Belliot, T. Daemen, D. D. Lasic, *Adv. Drug Delivery Rev.* **1995**, *17*, 31.
[12] D. Oupicky, M. Ogris, K. A. Howard, P. R. Dash, K. Ulbrich, L. W. Seymour, *Mol. Ther.* **2002**, *5*, 463.
[13] H. F. Liang, C. T. Chen, S. C. Chen, A. R. Kulkarni, Y. L. Chiu, M. C. Chen, H. W. Sung, *Biomaterials* **2006**, *27*, 2051.
[14] J. A. Champion, Y. K. Katare, S. Mitragotri, *J. Controlled Release* **2007**, *121*, 3.
[15] Y. Geng, P. Dalhaimer, S. S. Cai, R. Tsai, M. Tewari, T. Minko, D. E. Discher, *Nat. Nanotechnol.* **2007**, *2*, 249.
[16] X. L. Huang, X. Teng, D. Chen, F. Q. Tang, J. Q. He, *Biomaterials* **2010**, *31*, 438.
[17] N. S. Lee, L. Y. Lin, W. L. Neumann, J. N. Freskos, A. Karwa, J. J. Shieh, R. B. Dorshow, K. L. Wooley, *Small* **2011**, *7*, 1998.
[18] S. Venkataraman, J. L. Hedrick, Z. Y. Ong, C. Yang, P. L. Rachel Ee, P. T. Hammond, Y. Y. Yang, *Adv. Drug Delivery Rev.* **2011**, *63*, 1228.
[19] T. Chen, X. Guo, X. Liu, S. Shi, J. Wang, C. L. Shi, Z. Y. Qian, S. B. Zhou, *Adv. Healthc. Mater.* **2012**, *1*, 214.
[20] H. Herd, N. Daum, A. T. Jones, H. Huwer, H. Ghandehari, C. M. Lehr, *ACS Nano* **2013**, *7*, 1961.
[21] S. Barua, J. W. Yoo, P. Kolhar, A. Wakankar, Y. R. Gokarn, S. Mitragotri, *Proc. Natl. Acad. Sci. USA* **2013**, *110*, 3270.
[22] J. V. Natarajan, A. Darwitan, V. A. Barathi, M. Ang, H. M. Htoon, F. Boey, K. C. Tam, T. T. Wong, S. S. Venkatraman, *ACS Nano* **2014**, *8*, 419.
[23] T. Nomoto, S. Fukushima, M. Kumagai, K. Machitani, Arnida, Y. Matsumoto, M. Oba, K. Miyata, K. Osada, N. Nishiyama, K. Kataoka, *Nature Commun.* **2014**, *5*, 3545.
[24] P. Cossart, *J. Clin. Invest.* **1997**, *99*, 2307.
[25] S. E. A. Gratton, P. A. Ropp, P. D. Pohlhaus, L. J. Christopher, V. J. Maddenet, M. E. Napier, J. M. DeSimone, *Proc. Natl. Acad. Sci. USA* **2008**, *105*, 11613.
[26] M. J. Ernsting, M. Murakami, A. Roy, S. D. Li, *J. Controlled Release* **2013**, *172*, 782.
[27] Z. Liu, W. B. Cai, L. N. He, N. Nakayama, K. Chen, X. M. Sun, X. Y. Chen, H. J. Dai, *Nat. Nanotechnol.* **2007**, *2*, 47.

[28] J. H. Park, G. Maltzahn, L. L. Zhang, M. P. Schwartz, E. Ruoslahti, S. N. Bhatia, M. J. Sailor, *Adv. Mater.* **2008**, *20*, 1630.
[29] H. F. Yu, C. Dong, W. M. Zhou, T. Kobayashi, H. Yang, *Small* **2011**, *7*, 3039.
[30] T. Permpool, A. Sirivat, D. Aussawasathien, *Polym. Int.* **2014**, *63*, 2076.
[31] D. Dendukuri, P. S. Doyle, *Adv. Mater.* **2009**, *21*, 4071.
[32] H. G. Cui, Z. Y. Chen, S. Zhong, K. L. Wooley, D. J. Pochan, *Science* **2007**, *317*, 647.
[33] Z. M. Zhou, A. C. Anselmo, S. Mitragotri, *Adv. Mater.* **2013**, *25*, 2723.
[34] Z. B. Li, E. Kesselman, Y. Talmon, M. A. Hillmyer, T. P. Lodge, *Science* **2004**, *306*, 98.
[35] L. Cutlar, A. Aied, Y. Gao, U. Greiser, E. M. Murauer, D. Zhou, W. Wang, *Biomater. Sci.* **2015**, DOI: 10.1039/c5bm00216h.
[36] J. Y. Huang, Y. Gao, L. Cutlar, J. O'Keeffe-Ahern, T. Zhao, F. H. Lin, D. Zhou, S. McMahon, U. Greiser, W. Wang, W. Wang, *Chem. Commun.* **2015**, *51*, 8473.
[37] B. Newland, Y. Zheng, J. Yao, M. Abu-Rub, H. Cao, W. Wang, A. Pandit, *J. Am. Chem. Sci.* **2012**, *134*, 4782.
[38] N. Fairley, B. Hoang, C. Allen, *Biomacromolecules* **2008**, *9*, 2283.
[39] H. Y. Huang, R. Hoogenboom, M. A. M. Leenen, P. Guillet, A. M. Jonas, J. F. Gohy, U. S. Schubert, H. F. Gohy, *J. Am. Chem. Soc.* **2006**, *128*, 3784.
[40] Q. Yan, Y. Zhao, *Angew. Chem.* **2013**, *125*, 10132.
[41] P. Bhargava, Y. F. Tu, J. X. Zheng, H. M. Xiong, R. P. Quirk, S. Z. D. Cheng, *J. Am. Chem. Soc.* **2007**, *129*, 1113.
[42] H. J. Dou, M. Jiang, H. S. Peng, D. Y. Chen, Y. Hong, *Angew. Chem. Int. Ed.* **2003**, *42*, 1516.
[43] W. N. He, J. T. Xu, B. Y. Du, Z. Q. Fan, X. S. Wang, *Macromol. Chem. Phys.* **2010**, *211*, 1909.
[44] S. E. Burke, A. Eisenberg, *Langmuir* **2001**, *18*, 8341.
[45] H. Shen, A. Eisenberg, *Macromolecules* **2000**, *33*, 2561.
[46] K. Kataoka, T. Matsumoto, M. Yokoyama, T. Okano, Y. Sakurai, S. Fukushima, K. Okamoto, G. S. Kwon, *J. Controlled Release* **2000**, *64*, 143.
[47] M. Prabaharan, J. J. Grailer, S. Pilla, D. A. Steeber, S. Gong, *Biomaterials* **2009**, *30*, 3009.
[48] X. Guo, C. L. Shi, J. Wang, S. B. Di, S. B. Zhou, *Biomaterials* **2013**, *34*, 4544.
[49] Y. Yan, A. P. R. Johnston, S. J. Dodds, M. M. J. Kamphuis, C. Ferguson, R. G. Parton, E. C. Nice, F. Caruso, *ACS Nano* **2010**, *4*, 2928.
[50] R. Agarwal, V. Singh, P. Jurney, L. Shi, S. V. Sreenivasan, K. Roy, *Proc. Natl. Acad. Sci. USA* **2013**, *110*, 17247.
[51] P. F. Liu, Y. M. Sun, Q. Wang, Y. Sun, H. Li, Y. R. Duan, *Biomaterials* **2014**, *35*, 760.
[52] T. G. Iversen, T. Skotland, K. Sandvig, *Nano Today* **2011**, *6*, 176.
[53] L. Pelkmans, D. Puntener, A. Helenius, *Science* **2002**, *296*, 535.
[54] N. Doshi, A. S. Zahr, S. Bhaskar, J. Lahann, S. Mitragotri, *Proc. Natl. Acad. Sci. USA* **2009**, *106*, 21495.
[55] X. P. Duan, Y. P. Li, *Small* **2013**, *9*, 1521.
[56] J. Fang, H. Nakamura, H. Maeda, *Adv. Drug Delivery Rev.* **2011**, *63*, 136.
[57] P. M. Peiris, L. Bauer, R. Toy, R. Tran, J. Pansky, E. Doolittle, E. Schmidt, E. Hayden, A. Mayer, R. A. Keri, M. A. Griswold, E. Karathanasis, *ACS Nano* **2012**, *6*, 4157.
[58] J. H. Park, G. V. Maltzahn, L. L. Zhang, A. M. Derfus, D. Simberg, T. J. Harris, E. Ruoslahti, S. N. Bhatia, M. J. Sailoret, *Small* **2009**, *5*, 694.
[59] Z. Zhang, Q. Q. Qu, J. R. Li, S. B. Zhou, *Macromol. Biosci.* **2013**, *13*, 789.
[60] Q. Zhou, X. Guo, T. Chen, Z. Zhang, S. J. Shao, C. Luo, J. R. Li, S. B. Zhou, *J. Phys. Chem. B* **2011**, *115*, 12662.
[61] X. Guo, C. L. Shi, G. Yang, J. Wang, Z. H. Cai, S. B. Zhou, *Chem. Mater.* **2014**, *26*, 4405.